CHIN. PHYS. LETT. Vol. 38, No. 1 (2021) 016802 **Express Letter**

Dynamic Crossover in Metallic Glass Nanoparticles

Shan Zhang(张珊)[1], Weihua Wang(汪卫华)[2], and Pengfei Guan(管鹏飞)[1*]

[1]*Beijing Computational Science Research Center, Beijing 100193, China*
[2]*Institute of Physics, Chinese Academy of Sciences, Beijing 100190, China*

(Received 9 December 2020; accepted 24 December 2020; published online 29 December 2020)

We report the dynamic crossover behavior in metallic glass nanoparticles (MGNs) with the size reduction based on the extensive molecular dynamics (MD) simulations combined with the activation-relaxation technique (ART). The fragile-to-strong transition of dynamics can be achieved by just modulating the characteristic size of MGNs. It can be attributed to the abnormal fast surface dynamics enhanced by the surface curvature. By determining the potential energy surface, we reveal the hierarchy-to-flat transition of potential energy landscape (PEL) in MGNs, and demonstrate the intrinsic flat potential landscape feature of the MGN with size smaller than a critical size. Our results provide an important piece of the puzzle about the size-modulated potential energy landscape and shed some lights on the unique properties of MGs in nanoscale.

DOI: 10.1088/0256-307X/38/1/016802

The amorphous nature of metallic glasses (MGs) and their unique properties, such as high strength, hardness, and excellent soft magnetic properties, have attracted significant scientific and technological interests[1−8] in terms of structural and functional applications. Recently, tremendous research efforts have been dedicated to the fundamental studies of their various properties[9−11] and the related applications[12,13] in microscale, especially in nanoscale. A series of experiments[14,15] and simulations[16,17] suggest that MGs in nanoscale with high surface-volume ratio can exhibit qualitatively different behaviors from the bulk one, which extend the new areas of their applications in catalysis, composite reinforcement, additive manufacturing and biomedicine.[18−22] In the *in situ* transmission electron microscope experiments,[23,24] amorphous metallic nanoparticles present extreme thermostability and are further confirmed by the free energy analysis based on the Frenkel–Ladd methods.[25] The high-temperature coalescence and related underlying mechanisms of metallic glass nanoparticles have been studied at atomic-scale by *in situ* aberration-corrected transmission electron microscopy.[26] Recently, simulation works[27−29] suggest that the loosely packed, liquid-like surface layers with faster dynamics play a dominant role on the strong size dependence of the atomic structure, dynamics, and glass transition temperature in low-dimensional MGs. Gong *et al.*[30] reported the intrinsic features of the ideal glass by investigating the thermodynamic properties and potential energy surface of the Al clusters with dozens of atoms. By modulating the PEL flatness,[31] the glass transitions were found to be independent of the structure symmetry of nanoparticles. On the basis of previous works, it can be generally perceived that metallic glasses in nanoscale provide a new perspective on comprehensive understanding of their properties and related mechanisms. However, the shell-dependent dynamics and the related properties of potential energy surface over a large range of particle size remain largely unknown, although fast surface dynamics of nanostructured MGs have widely been observed in both experiments[24,28,32] and simulations.[33,34]

In this Letter, we study the particle size-dependent dynamics properties of MGNs by performing the molecular dynamics (MD) simulations in various model metallic glasses. A critical size (D_c) for the dynamic crossover can be observed by collecting the particle-size dependent kinetic fragility, which characterizes the way in which the structural relaxation times change with reciprocal temperature. The fragile-to-strong transition can be achieved by just modulating the nanoparticle size. It can be attributed to the curvature-dependent fast surface dynamics in the MGNs. By determining the potential energy surface with the ART method,[35] we demonstrate that the MGN with dozens of atoms behaves an intrinsic flat potential landscape,[35] which is quite distinct from the one that has a size larger than the critical size.

We performed the molecular dynamics simulations in typical binary model CuZr metallic glasses using the open-source code LAMMPS.[36] To obtain general conclusions, two embedded atom method potentials of CuZrAl[37] and CuZr[38] were employed to describe the interatomic interactions in two simulated systems

Supported by the Science Challenge Project (Grant No. TZ2018004), and the National Natural Science Foundation of China (Grant No. U1930402). S.Z. and P.G. acknowledge the computational support from the Beijing Computational Science Research Center (CSRC).
*Corresponding author. Email: pguan@csrc.ac.cn
© 2021 Chinese Physical Society and IOP Publishing Ltd

of $Cu_{50}Zr_{50}$ (at.%) and the $Cu_{86}Zr_{14}$ (at.%), respectively. To evaluate the particle size effects, we carried out a wide range of simulations in different-size MGNs. These MGNs, with diameters of 0.8, 1, 1.3, 1.5, and 3 nm, located in the center of a large cubic box (∼15 nm) under periodic boundary conditions in three dimensions. A serial of spherical MGNs with surrounding vacuum can be prepared under the canonical (NVT) ensemble due to the surface tension. To examine the behavior in the large system, we also prepared the bulk sample (containing of 5000 atoms) for comparison. The time step was set to 2 fs. First, we equilibrated the samples at 1300 K for at least 1 ns. After being quenched to the target temperatures, we relaxed the systems to equilibrium and collected at least 10^4 configurations for dynamic analysis. The related inherent structures of MGNs were obtained by the conjugate gradient (CG) algorithm. We used the ART method to explore the potential energy hypersurfaces of each inherent structure. Our model systems and ART details are presented in the Supporting Information.

To explore the particle size's influences on the relaxation dynamics in the atomic level, we measured the structural relaxation time τ_α by calculating the self-intermediate scattering function (SISF) for different sized MGNs. The definition of SISF can be expressed as

$$F_s(q,t) = \frac{1}{N}\Big\langle \sum_{l=1}^{N} \exp -i\boldsymbol{q}\cdot[\boldsymbol{r}_l(t) - \boldsymbol{r}_l(0)]\Big\rangle,$$

where N is the number of the systems, q is the wave vector, and $\boldsymbol{r}_l(t) - \boldsymbol{r}_l(0)$ represents the displacement vector of atom l over a given time interval t, $\langle\cdots\rangle$ denotes the ensemble average over different configurations. The SISF curves for a series of MGNs with represented sizes and the referenced bulk one at $T = 1300$ K and $T = 800$ K are shown in Fig. 1(a). The collapses of SISFs in a short-time regime suggest that the statistical behavior of the local structure packing is insensitive to the particle size because of the short-time relaxation in correlated with the cage effect. The major differences appear in the long-time alpha-relaxation regime. At the high temperature ($T = 1300$ K), the MGNs with different sizes have slightly different relaxation behaviors, which suggest the small particle-size effect of the dynamics at high temperature. However, at the low temperature (800 K), the two-step decay[39] becomes significant and the large deviation indicates the stronger size-dependent structural relaxation time.

The characteristics of τ_α, representing the relaxation dynamics, which is usually defined as the time until the $F_s(q,t)$ decays to $1/e$, are shown in Fig. 1(b) for all investigated MGNs and the referenced bulk one. In general, the smaller MGN presents faster dynamics, which is consistent with the previous studies.[27,29] The Vogel–Fulcher–Tammann (VFT) function[40] $\tau = \tau_0 \cdot \exp[BT_0/(T - T_0)$ was employed to fit the data, where τ_0, B, and T_0 are the fitting parameters and are empirical material-dependent. The glass transition temperature T_g is defined as $\tau(T = T_g) = 10^4$ ps. The extracted T_g decreases with the size decreasing, which is totally in agreement with the previous studies.[29,34] The way of the abrupt slowdown of structural relaxation approaching T_g is believed to be important for understanding the underlying physics of glass transition. The widely used *fragility* classification scheme introduced by Angell[41] defines how the structural relaxation times change with reciprocal temperature scaled to a characteristic temperature. Here we choose the T_g as the characteristic temperature, and the τ_α as a function of T_g-scaled temperature for different-sized MGNs is shown in Fig. 1(c). It is surprising to find that the scaled curves of MGNs with $D \geqslant 1.5$ nm are collapsed into the bulk curve, which implies that all these systems behave identical underlying physics of dynamics slowdown. However, for $D < 1.5$ nm, the scaled curve approaches to line relation, which means that there is a critical size D_c for the dynamic crossover in the MGNs. This phenomenon is independent of the chemical composition and the interatomic potential (see Figs. S3 and S5 in the Supporting Information), except for the possible change of D_c.

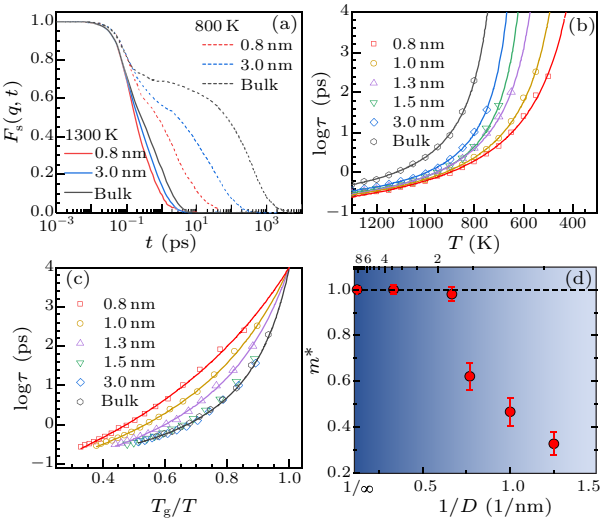

Fig. 1. (a) The self-intermediate scattering functions of the various-size (the bulk MGs and the diameter with 1.3 and 0.8 nm MGNs) systems at high ($T = 1300$ K) and low ($T = 800$ K) temperatures. (b) The relaxation time τ_α versus temperature T at the different sizes of samples. The solid lines are the VFT function fitting. (c) The Angell plot of relaxation time τ_α versus T_g/T for various systems. The solid lines are the T_g/T-scaled VFT function fitting, where the size is larger than 1.5 nm and the data are collapsed. (d) Size-dependent normalized fragility index m^*. The dashed line represents the inherent fragility value. The sizes in (b)–(d) are 0.8, 1.0 1.3, 1.5, 3.0 nm, and bulk one.

We define the kinetic fragility m as the slope of the

τ_α curves at T_g by

$$m = \frac{d\log\tau}{dT_g/T}\Big|_{T_g}.$$

To quantitatively characterize this size-dependent crossover behavior, we select the kinetic fragility of the bulk sample, m_{bulk}, as the reference. Figure 1(d) shows the normalized kinetic fragility $m^* = m/m_{bulk}$ as a function of the particle size D. It is clear that the $m^* = 1$ for larger-sized MGNs and starts to be smaller than 1 as the particle size D reduced to 1.5 nm. The m^* reduces rapidly with the decrease of particle size D, even decreases to 0.33 at the size of 0.8 nm. This indicates that the fragile-to-strong transition of relaxation dynamics can be achieved just by modulating the particle size. This also implies that the underlying physics of dynamics slowdown in MGNs system begins to deviate from the bulk system markedly as the particle size $D < D_c$.

To reveal the underlying mechanisms of this particle-size modulated dynamic crossover, we further analyzed the atomic-level details of selected MGNs with a wide range of diameter (1.0 nm, 1.3 nm, 1.5 nm, and 3.0 nm). As shown in Fig. S4, the atomic number density distribution of MGNs exists the core-shell behavior.[29] The deviation of the chemical distribution on the surface shell is negligible. This means that there is no surface chemical segregation and the chemical heterogeneity is not the influent factor of the size-modulated transition. To investigate the surface dynamic behaviors in different-sized MGNs, we calculate the related SISF by tracking the trajectory of atoms in the surface shell and inner shells (see the Supporting Information for details). As shown in Fig. S6, the surface shell generally exhibits faster dynamics than the inner shells, which is consistent with the previous work.[29] However, the temperature dependences of the surface dynamics in MGNs with different D are completely different. As shown in Fig. 2(a), the SISF of surface shell is almost certainly identical in all MGNs at high temperature, which is different from the total dynamics of all atoms [Fig. 1(a)]. This means that the fast surface dynamics does not exit curvature effect at high temperature and the dynamics of inner shells should behave remarkable size effect. However, as the temperature decreases, the curvature effect is developed and the two-step decay[39] becomes significant with the curvature $(1/D)$ decreasing. As we plotted the Angell plot of the surface dynamics (τ_s) of different-sized MGNs [Fig. 2(b)], it is surprising for us to find the collapse of the data for MGNs with $D > D_c$. We also observed the similar fragile-to-strong transition of the surface dynamics as the total dynamics [Fig. 1(c)]. It indicates the pronounced curvature effect of the fast surface dynamics in sub-nm-sized MGNs and the curvature-dependent fast surface dynamics should play the key role for understanding the size-modulated fragile-to-strong transition.

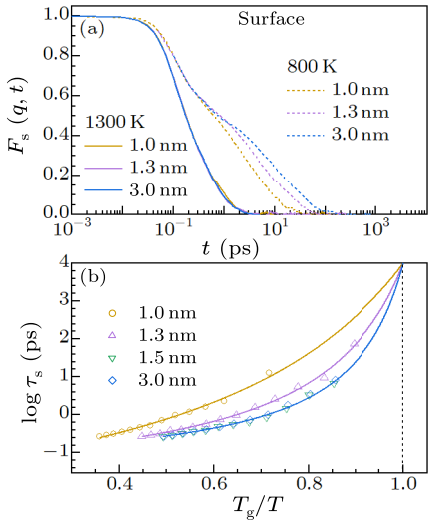

Fig. 2. (a) The surface SISF of the various size MGNs at 1300 K (solid line) and 800 K (dashed line). The size range is 1.0, 1.3, and 3.0 nm. (b) The Angell plot of relaxation time τ_s versus T_g/T for various surface systems. The solid lines are the T_g/T-scaled VFT function fitting, where the size is larger than 1.5 nm and the data are collapsed.

To further understand the curvature effect on the fragility transition, we collect the dynamics of surface-shell (τ_s) and inner shells (τ_i) in different-sized MGNs in Fig. 3. The total dynamics (τ_t) of the bulk sample and the 0.8-nm-sized MGNs with only one shell are plotted for reference. It is found that the curves of $\tau_t(D = 0.8\,\text{nm})$ and $\tau_t(\text{bulk})$ define the upper and lower boundaries of the relaxation dynamics, respectively. At high temperature, the data of surface dynamics τ_s collapse to the curves of $\tau_t(D = 0.8\,\text{nm})$, and the data of inner dynamics τ_i collapse to the curves of $\tau_t(\text{bulk})$. However, as the temperature decreases, the data of MGNs begin to deviate from the master curves, except the data of $\tau_s(D = 1.0\,\text{nm})$. It confirms the curvature effects not only in the inner dynamics but also in the surface dynamics at low temperature. The overlap between the $\tau_s(D = 1.0\,\text{nm})$ and $\tau_t(D = 0.8\,\text{nm})$ indicates that the curvature effect of surface dynamics reaches a saturation state in ultra-small MGNs. The decoupling between τ_s and τ_i, and the curvature-dependent fast surface dynamics give us some hints for understanding the size-modulated fragile-to-strong transition of relaxation dynamics. As the MGN size decreases, the weight of τ_s increases due to the higher surface-volume ratio and the dynamics behaviors are dominated by τ_s in ultra-small MGNs. Since the kinetic fragility of τ_s can be modulated by the surface curvature, the size-modulated fragility transition is contributed by the synergistic influences between the surface-volume ratio and the curvature-dependent surface dynamics. Moreover, the data of $\tau_t(0.8)$, $\tau_s(1.0)$ and $\tau_i(10)$ exhibit almost linear relation with the $1/T$, which implies that the dynam-

ics of ultra-small MGNs are close to the simple liquids. This suggests that the features of ultra-small MGNs should be completely different from the large systems.

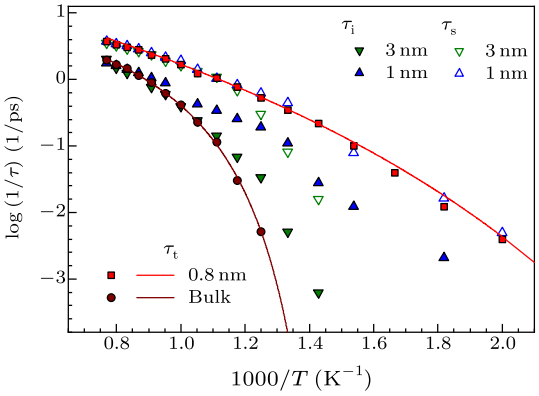

Fig. 3. The relaxation time as a function of $1000/T$ in various-size MGs. The brown and red symbols represent the relaxation behavior of the 0.8 nm sample and the bulk system, respectively. The solid line is the scaled-VFT fitting. The green and blue open symbols represent the surface relaxation behavior of the 1.0 nm and 3.0 nm samples, respectively. The solid symbols represent the relaxation behavior of their inner atoms.

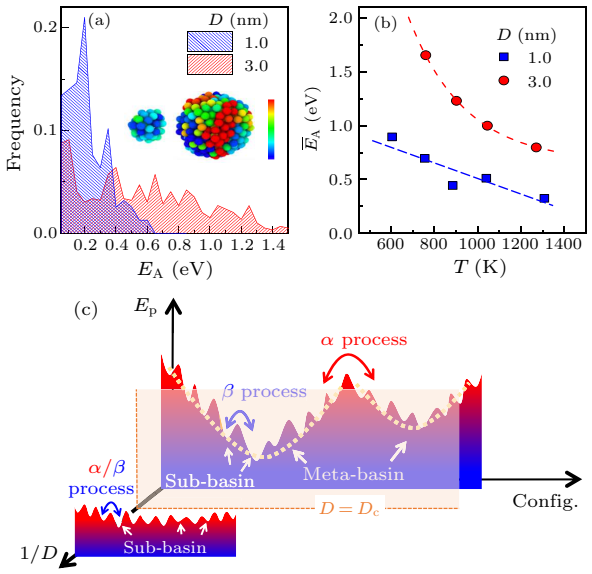

Fig. 4. (a) The distribution of activation energy of the 1.0 nm and 3.0 nm MGNs. The insets show the distribution of their average atomic arithmetic activation energy. (b) The average effective activation energy of 1.0 nm and 3.0 nm MGNs versus temperature. (c) The schematic diagram of PEL morphology with size reduction in configuration space.

According to the PEL perspective,[42,43] the kinetic fragility of relaxation dynamics is determined by the intrinsic features of potential energy surface (PES). When the liquid exhibits the Arrhenius behavior as a strong liquid, the activation energy of the relaxation process $E = d\ln\eta/d(\frac{1}{T})$ should be a constant. However, the activation energy of the fragile liquid increases as the temperature approaching to the glass transition temperature (T_g)[43] due to the enhanced cooperative motions. By performing the ART in our MD simulations, we measured the activation energy (E_A) spectra to explore the local features of PES. The calculated E_A spectra are shown in Fig. 4(a) for 1-nm-sized ($<D_c$) and 3-nm-sized ($>D_c$) MGNs with distinct kinetic fragility. The E_A spectra of the 1-nm-sized MGN shift to the left side and the distribution are much narrower than the 3-nm-sized one. The spatial distributions of arithmetic mean E_A of each atom, $\overline{E}_{A,k}$ in different MGNs (see the Supporting Information for the details of the method) are shown in the inserts of Fig. 4(a). The 1-nm-sized MGN behaves small value and tiny fluctuation of E_A, comparing to the 3-nm-sized one. To reveal the energy state dependence of the local PES features, we monitored the E_A spectra of two sets of MGNs with different D, which are quenched from various parent temperature T_P, in Fig. S9. As the T_P decreases, the E_A distribution generally shifts towards the right side and develops a wide distribution. The related effective E_A (see the Supporting Information for more details), to characterize the statistic properties, is calculated by[44]

$$\overline{E}_A(E_{IS,T}) = k_B T \cdot \ln\left[\int P(E_A|E_{IS}) e^{\frac{E_A}{k_B T}} dE_A\right].$$

As we plotted $\overline{E}_A$ as a function of T_P, it is interesting to find the distinct dependences of $\overline{E}_A$ in 1-nm-sized and 3-nm-sized MGNs. For the 1-nm-sized MGN, the $\overline{E}_A$ increases linearly and gently with T_P decreasing. However, the $\overline{E}_A$ presents dramatic increase as the T_P decreases in 3-nm-sized MGN. The results are consistent with the kinetic fragility m, which indicates that the system becomes stronger with the particle size reduction. Moreover, as we analyzed the number of atoms involved in every activation event [Fig. S8(b)], it is amazing to find that the averaged atomic number is ~40. This implies that each "local" activation event triggered by ART is a global (α) relaxation process with ~80% atoms activated in 1-nm-sized MGNs. It means that the β and α relaxation processes are almost identical in ultra-small-sized MGNs. Thus, we can illustrate the PEL morphology with the nanoparticle size in Fig. 4(c). As the particle size larger than the critical size D_c, the PEL topography behaves intrinsic hierarchy as the bulk system,[45] which is constructed by well-separated meta-basins, consisting of relatively deep sub-basins. With the nanoparticle size D smaller than D_c, the hierarchical nature begins to disappear and the PEL becomes intrinsic flat in sub-nm systems, which is constructed by shallow sub-basins with similar depths. Thus, the fast coalescence of MGNs[26] is originated from their simple-liquid-like flat PEL. Moreover, it is of particular interest to reconsider the previous conclusions[29] about the intrinsic flat potential landscape feature of ideal glass with dozens of atoms.

In summary, a fragile-to-strong crossover of relax-

ation dynamics and the hierarchy-to-flat transition of PEL have been observed by modulating the characteristic size of MGNs. By systematically analyzing the shell-dependent dynamics, the curvature influence of the fast surface dynamics has been revealed. The degeneracy of β and α processes is developed as the characteristic size reduces to a critical size. The intrinsic feature of the MGN with dozens of atoms is a flat potential landscape. The dynamic behavior of the ultra-small MGN should be similar to a simple liquid. Thus, we provide the underlying physics of the unique properties of the sub-nm MGNs and shed some lights on the nature of glass and glass transition.

References

[1] Chen D Z, Jang D, Guan K M, An Q, Goddard W A and Greer J R 2013 *Nano Lett.* **13** 4462
[2] Jang D and Greer J R 2010 *Nat. Mater.* **9** 215
[3] Volkert C A, Donohue A and Spaepen F 2008 *J. Appl. Phys.* **103** 083539
[4] Lee S W, Jafary-Zadeh M, Chen D Z, Zhang Y W and Greer J R 2015 *Nano Lett.* **15** 5673
[5] Brower W E, Matyjaszczyk M S, Pettit T L and Smith G V 1983 *Nature* **301** 497
[6] Pauly S, Löber L, Petters R, Stoica M, Scudino S, Kühn U and Eckert J 2013 *Mater. Today* **16** 37
[7] Shen Y, Li Y, Chen C and Tsai H J M 2017 *Mater. & Des.* **117** 213
[8] Zberg B, Uggowitzer P J and Löffler J F 2009 *Nat. Mater.* **8** 887
[9] Wang W H, Dong C and Shek C H 2004 *Mater. Sci. Eng. R* **44** 45
[10] Van Der Scheer P, Van De Laar T, Van Der Gucht J, Vlassopoulos D and Sprakel J 2017 *ACS Nano* **11** 6755
[11] Li Q J, Xu B, Hara S, Li J and Ma E 2018 *Acta Mater.* **145** 19
[12] Inoue A and Nishiyama N 2007 *MRS Bull.* **32** 651
[13] Schroers J, Kumar G, Hodges T, Chan S and Kyriakides T 2009 *JOM* **61** 21
[14] Dong J, Feng Y H, Huan Y, Yi J, Wang W H, Bai H Y and Sun B A 2020 *Chin. Phys. Lett.* **37** 017103
[15] Jang D, Gross C T and Greer J R 2011 *Int. J. Plast.* **27** 858
[16] Şopu D, Foroughi A, Stoica M and Eckert J 2016 *Nano Lett.* **16** 4467
[17] Stevenson J D and Wolynes P G 2008 *J. Chem. Phys.* **129** 234514
[18] Kumar G, Desai A and Schroers J 2011 *Adv. Mater.* **23** 461
[19] Chen N, Frank R, Asao N, Louzguine-Luzgin D V, Sharma P, Wang J Q, Xie G Q, Ishikawa Y, Hatakeyama N, Lin Y C, Esashi M, Yamamoto Y and Inoue A 2011 *Acta Mater.* **59** 6433
[20] Witte R, Feng T, Fang J X, Fischer A, Ghafari M, Kruk R, Brand R A, Wang D, Hahn H and Gleiter H 2013 *Appl. Phys. Lett.* **103** 073106
[21] Ketov S V, Shi X, Xie G, Kumashiro R, Churyumov A Y, Bazlov A I, Chen N, Ishikawa Y, Asao N, Wu H and Louzguine-Luzgin D V 2015 *Sci. Rep.* **5** 7799
[22] Zhao M, Abe K, Yamaura S I, Yamamoto Y and Asao N 2014 *Chem. Mater.* **26** 1056
[23] Chen N, Wang D, Guan P F, Bai H Y, Wang W H, Zhang Z J, Hahn H and Gleiter H 2019 *Appl. Phys. Lett.* **114** 043103
[24] Cao C R, Huang K Q, Shi J A, Zheng D N, Wang W H, Gu L and Bai H Y 2019 *Nat. Commun.* **10** 1966
[25] An S, Su R, Zhao S, Liu J, Liu B and Guan P 2018 *Phys. Rev. B* **98** 134101
[26] Tian Y, Jiao W, Liu P, Song S, Lu Z, Hirata A and Chen M 2019 *Nat. Commun.* **10** 5249
[27] Li Y Z, Sun Y T, Lu Z, Li M Z, Bai H Y and Wang W H 2017 *J. Chem. Phys.* **146** 224502
[28] Zhang P, Maldonis J J, Liu Z, Schroers J and Voyles P M 2018 *Nat. Commun.* **9** 1129
[29] Qi W and Bowles R K 2016 *ACS Nano* **10** 3416
[30] Sun D, Shang C, Liu Z and Gong X 2017 *Chin. Phys. Lett.* **34** 026402
[31] Sun D Y and Gong X G 2020 *New J. Phys.* **22** 103020
[32] Chen L, Cao C R, Shi J A, Lu Z, Sun Y T, Luo P, Gu L, Bai H Y, Pan M X and Wang W H 2017 *Phys. Rev. Lett.* **118** 016101
[33] Sun G, Saw S, Douglass I and Harrowell P 2017 *Phys. Rev. Lett.* **119** 245501
[34] Bi Q L, Lü Y J and Wang W H 2018 *Phys. Rev. Lett.* **120** 155501
[35] Mousseau N, Béland L K, Brommer P, Joly J F, El-Mellouhi F, Machado-Charry E, Marinica M C and Pochet P 2012 *J. At. Mol. Opt. Phys.* **2012** 925278
[36] Plimpton S 1995 *J. Comput. Phys.* **117** 1
[37] Cheng Y Q, Ma E and Sheng H W 2009 *Phys. Rev. Lett.* **102** 245501
[38] Mendelev M I, Sordelet D J and Kramer M J 2007 *J. Appl. Phys.* **102** 043501
[39] Kob W and Andersen H C 1995 *Phys. Rev. E* **52** 4134
[40] Rault J 2000 *J. Non-Cryst. Solids* **271** 177
[41] Angell C A 1995 *Science* **267** 1924
[42] Angell C A 1988 *J. Phys. Chem. Solids* **49** 863
[43] Debenedetti P G and Stillinger F H 2001 *Nature* **410** 259
[44] Wang Y J, Du J P, Shinzato S, Dai L H and Ogata S 2018 *Acta Mater.* **157** 165
[45] Wang B, Wang L J, Shang B S, Gao X Q, Yang Y, Bai H Y, Pan M X, Wang W H and Guan P F 2020 *Acta Mater.* **195** 611

Supporting Information for

Dynamic Crossover in Metallic Glass Nanoparticles

Shan Zhang (张珊) [1], Weihua Wang (汪卫华) [2], Pengfei Guan (管鹏飞) [1]

[1] *Beijing computational science research center, Beijing 100193, China*

[2] *Chinese Academy of Sciences, Institute of Physics, Beijing 100190, China*

1 The calculated self-intermediate scattering functions (SISF)

SISFs for $Cu_{50}Zr_{50}$ system. We have calculated the SISF of $Cu_{50}Zr_{50}$ metallic glass nanoparticles (MGNs, with the size of 0.8, 1.0, 1.3, 1.5, 3.0 nm) and bulk MG. With the size increases, the relaxation dynamics become slower.

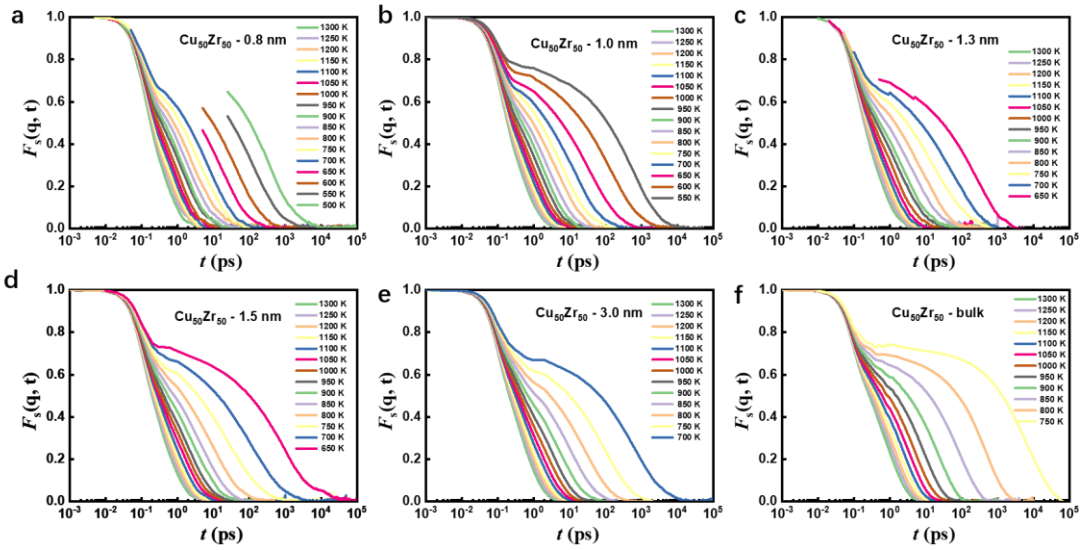

Fig.S1. The SISFs of $Cu_{50}Zr_{50}$ MGNs and bulk MG with various sizes at the different temperatures.

SISFs for $Cu_{86}Zr_{14}$ MGNs. We have calculated the SISF of $Cu_{86}Zr_{14}$ MGNs (with the size of 0.8, 1.0, 1.3, 1.5, 3.0 nm) and bulk MG. The trend is consistent with the $Cu_{50}Zr_{50}$ system.

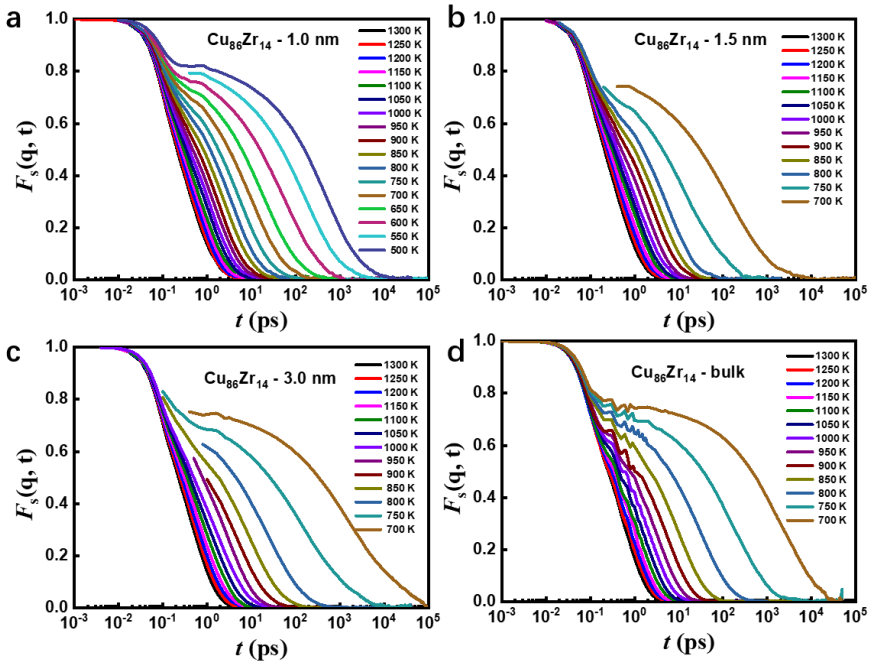

Fig.S2. The SISFs of $Cu_{86}Zr_{14}$ MGNs and bulk MG with various sizes at the different temperatures.

2 The Angell plots and normalized fragility index for $Cu_{86}Zr_{14}$ system

We plotted the Angell plots of the $Cu_{86}Zr_{14}$ system and observed the fragile-to-strong transition of dynamics. The critical size D_c is ~1.5 nm which indicates the composition-independent crossover behaviors of kinetic fragility.

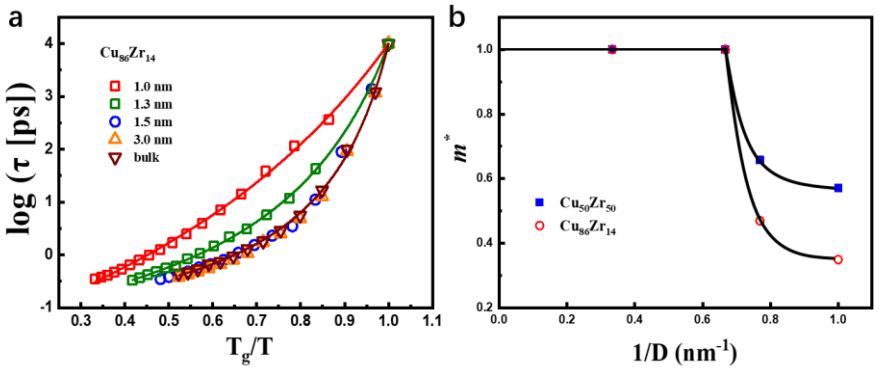

Fig. S3. (a) The Angell plots of relaxation time τ_α versus T_g/T in $Cu_{86}Zr_{14}$ system; (b) the normalized fragility index m* with 1/D for $Cu_{86}Zr_{14}$ and $Cu_{50}Zr_{50}$ systems.

3 The shell-dependent dynamics for the $Cu_{50}Zr_{50}$ system

The core-shell feature of MGNs. The core-shell feature is significant in the atomic configurations of MGNs. We defined the outermost shell as the surface shell and the rest part as the inner shells.

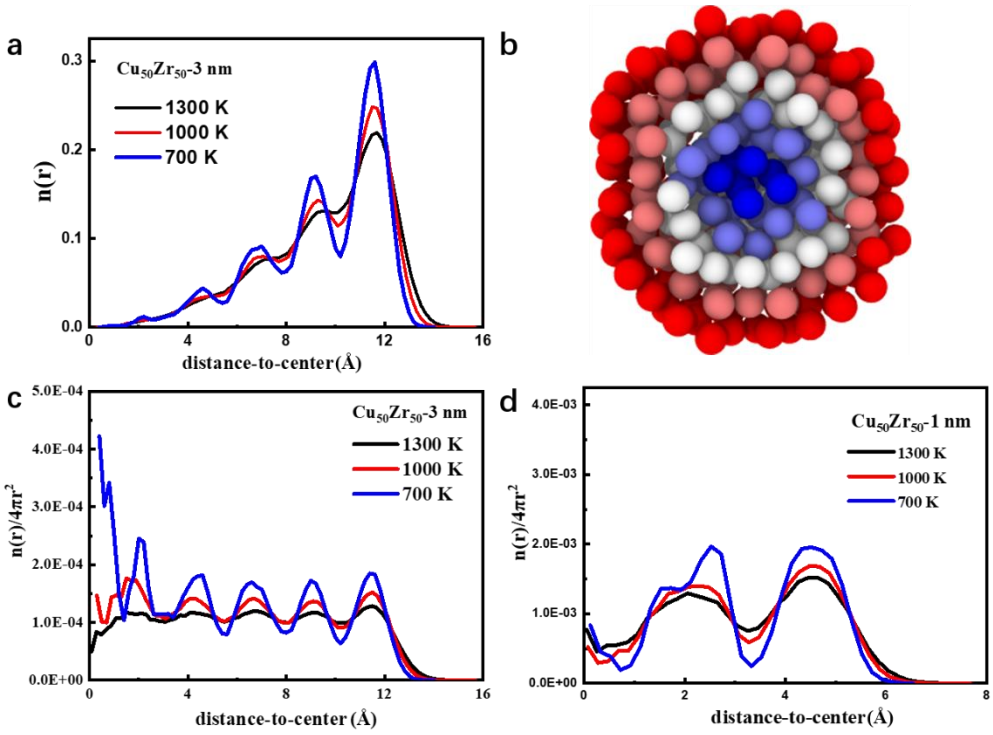

Fig. S4. (a) The number of atoms against the distance to the center at 700 K, 1000 K, and 1300 K for the 3.0 nm $Cu_{50}Zr_{50}$ systems. (b) The visualization diagram of the 3.0 nm $Cu_{50}Zr_{50}$ system with colored shells. (c) and (d) The number density in each shell at 700 K, 1000 K, and 1300 K for 3.0 nm and 1.0 nm $Cu_{50}Zr_{50}$ systems, respectively.

The element distribution in the surface shell. The surface mobility played an essential role in the dynamics of MGNs. We analyzed the atomic percent of Cu element in the surface shell of various MGNs (averaged 100 samples to reduce statistical errors). As shown in Fig. S5, there is no segregation of chemical components on the surface.

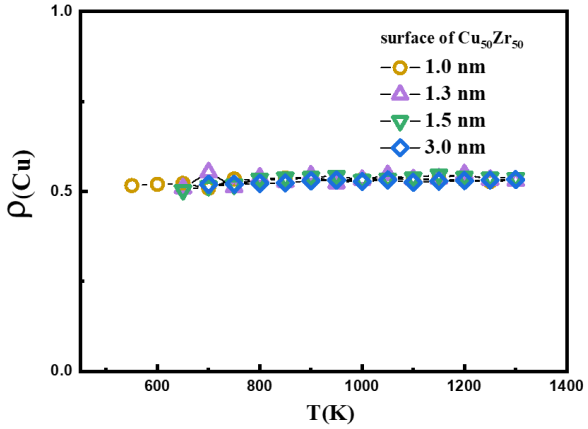

Fig. S5. The atomic percent of Cu element in the surface shell of $Cu_{50}Zr_{50}$ MGNs.

Shell-dependent relaxation dynamics. To examine shell-dependent dynamics in MGNs, we defined the SISF of various shells as:

$$F_{s,L}(Q,t) = \frac{1}{N}\langle \sum_{l=1}^{N} exp\{-iQ \cdot [r_l(t,L) - r_l(0,L)]\}\rangle \quad (1)$$

where N is the number of particles in the L-shell and $r_l(t,L)$ and $r_l(0,L)$ are the position of the atom in the L-shell at 0 and t time simultaneously. We plotted the SISFs of the surface shell and inner shells in 1.0 nm and 3.0 nm MGNs in Fig. S6. The surface relaxation time $\tau_{\alpha,s}$ as a function of temperature are shown in Fig. S7. The surface dynamics of MGNs are faster than the inner-shells. [1]

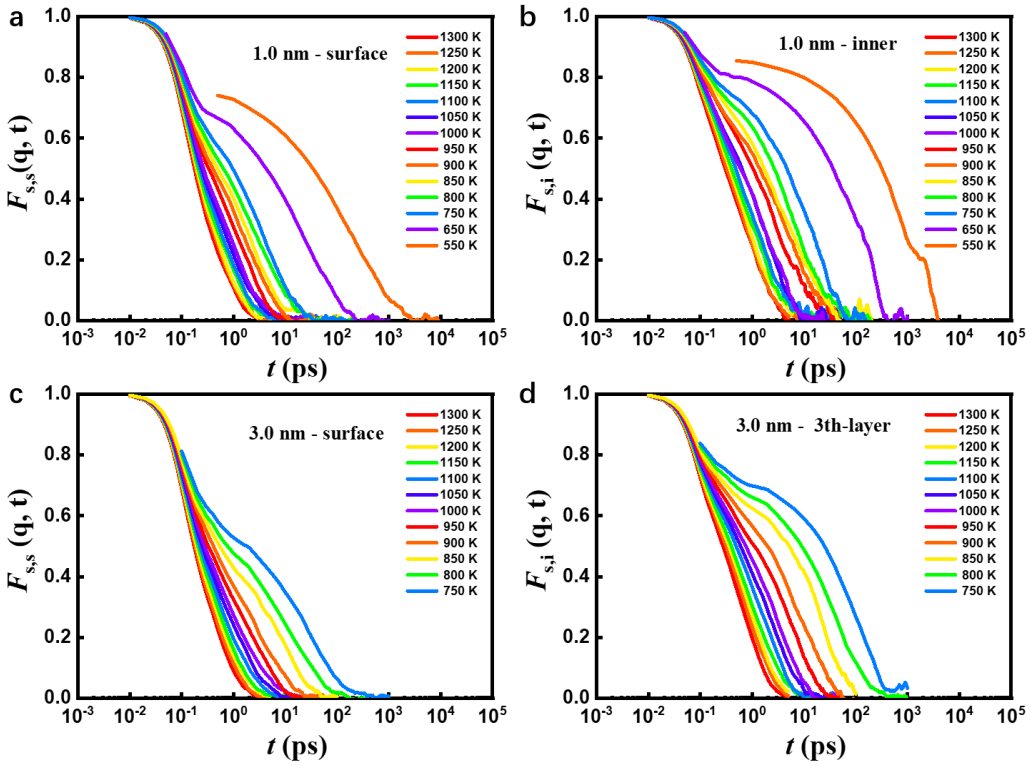

Fig. S6. The shell-dependent SISF of the 1.0 nm and 3.0 nm $Cu_{50}Zr_{50}$ MGNs at the different temperatures.

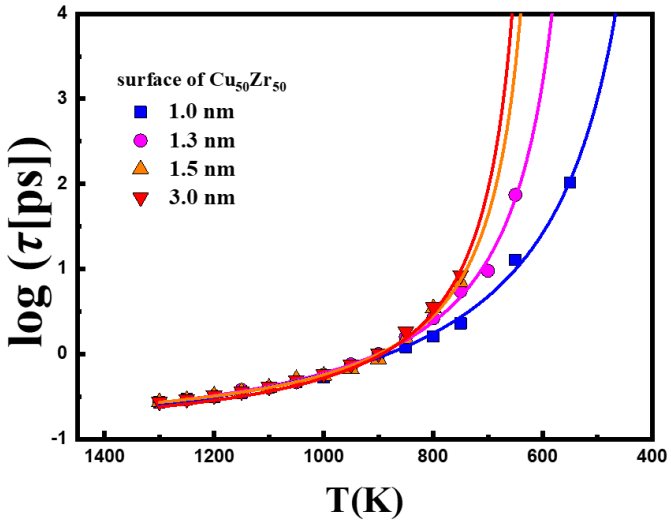

Fig. S7. The surface relaxation time $\tau_{\alpha,s}$ versus T of $Cu_{50}Zr_{50}$ MGNs. The solid curves are the VFT fitting curves.

4 E_A spectra and the effective barrier $\overline{E}_A$

E_A spectra. We employed CG algorithm to prepare the inherent structure of MGNs which is quenched from different parent temperatures instantaneously. To obtain the E_A spectrum, we applied 50 ~500 activation-relaxation technique (ART) searches for each group of atoms. We set the initial perturbation displacement of 0.5 Å and the direction of perturbation randomly in the searching events. The perturbation radius is 3.2 Å. And the force threshold is below 0.05 eV/Å. Thus, we could get the raw data by 25,000 ART searches for a given sample with 1nm and 3 nm at 600 K, 750 K, 900 K, 1050 K, and 1300 K. We should use two removal steps[2, 3] to obtain ~ 2,000 effective searches (in different samples, the number will be different). Finally, we can get the E_A spectrum for each sample. Because the temperature is up the glass transition temperature, we selected 5 and 10 configurations at each temperature for a statistical average. Figure S8 (a) shows the E_A spectra of MGNs with different sizes. With the size increasing, the distribution of activation energy has a broader range. In Fig. S9, we plotted the 1.0 nm and 3.0 nm samples' E_A spectra at various temperatures.

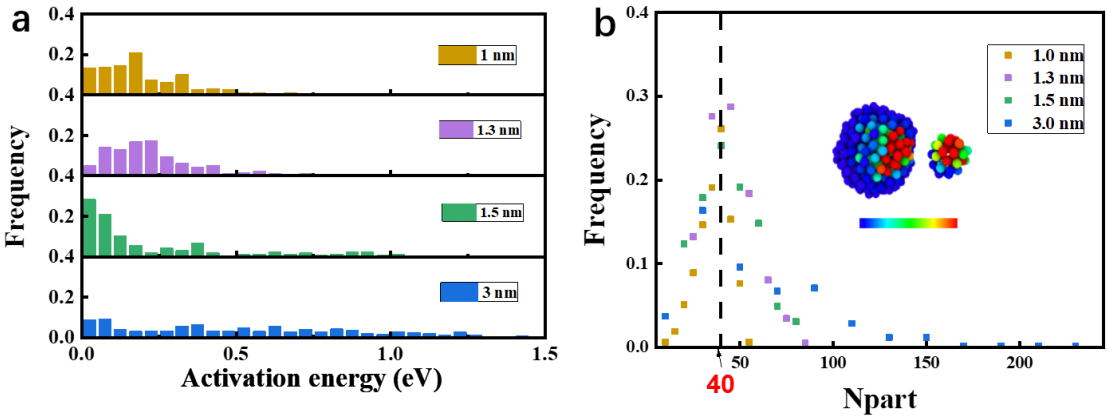

Fig. S8 (a) E_A spectra of 1.0 nm, 1.3 nm, 1.5 nm, and 3.0 nm $Cu_{50}Zr_{50}$ MGNs at 750 K. (b) Distribution of the number of atoms participating in activation event. The inset shows the distribution of atoms when the number of active atoms is ~40.

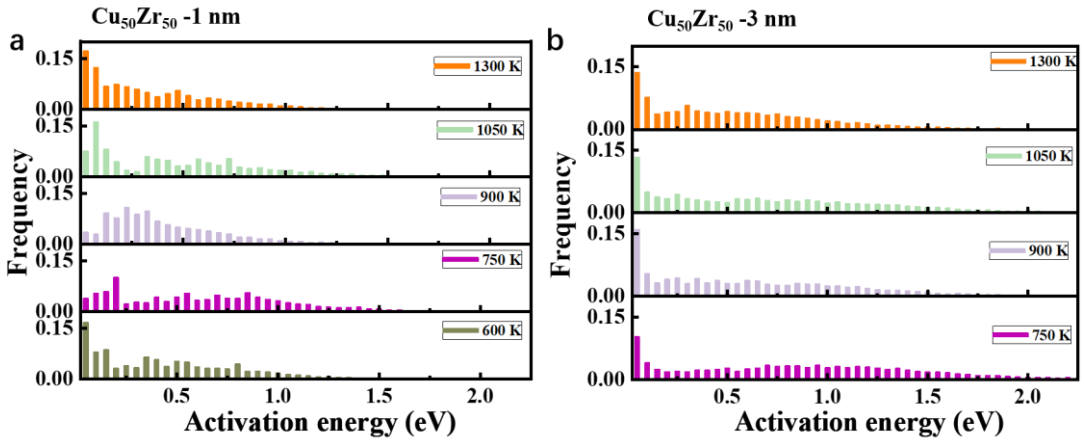

Fig. S9. E_A spectra of (a) 1.0 nm and (b) 3.0 nm $Cu_{50}Zr_{50}$ MGNs with various parent temperatures.

The arithmetic mean E_A, $\bar{E}_{A,k}$ and Effective barrier $\bar{E}_A$ The arithmetic mean of each atom's E_A, $\bar{E}_{A,k}$ is the arithmetic mean of all effective searches' activation energy E_A of k atom. It was calculated by Eq. (2)

$$\bar{E}_{A,k} = \frac{1}{N_{event\ ,k}} \sum_{i=1}^{N_{event\ ,k}} E_A(i,k) \tag{2}$$

where $E_A(i,k)$ is the k atom's activation energy in i^{th} event. $N_{event\ ,k}$ is the number of the effective events of k atom. The effective barrier was calculated by Eq. (3)[4] to keep high energy barriers dominate the diffusivity.

$$\bar{E}_A(E_{IS,T}) = k_B T \cdot \ln\left[\int P(E_A|E_{IS}) e^{\frac{E_A}{k_B T}} dE_A\right] \tag{3}$$

References

1. Chen N, Wang D, Guan P F, Bai H Y, Wang W H, Zhang Z J, Hahn H, & Gleiter H 2019 *Appl. Phys. Lett.* **114**.
2. Zhang S, Liu C, Fan Y, Yang Y, & Guan P 2020 *J. Phys. Chem. Lett.* **11** 2781.
3. Fan Y, Iwashita T, & Egami T 2014 *Nat. Commun.* **5**.
4. Wang Y-J, Du J-P, Shinzato S, Dai L-H, & Ogata S 2018 *Acta Mater.* **157** 165.